

Mesoscale modulation of marine boundary layer water vapor isotopologues during ~~EUREC4A~~EUREC⁴A

Joseph Galewsky¹ and Sebastian A. Los¹

¹Department of Earth and Planetary Sciences, University of New Mexico, Albuquerque, New Mexico

Correspondence: Joseph Galewsky (galewsky@unm.edu)

Abstract. Shallow cumulus clouds in trade-wind regions remain ~~a major~~an important source of uncertainty in climate projections, with ~~conflicting hypotheses about~~competing interpretations of how mesoscale circulations ~~affect~~influence boundary layer moisture. We analyze water vapor isotopologue measurements from the EUREC⁴A campaign to quantify ~~the~~mesoscale modulation of marine boundary layer humidity and ~~isotopic~~isotopic composition. Surface ~~δD~~ δD measurements from R/V ~~Meteor~~Meteor ~~show remarkably~~show a strong sensitivity to mesoscale vertical ~~motions, responding 7.5 times more strongly than~~humidity when normalized by observed standard deviations. Mesoscale upward motion counteracts velocity, substantially exceeding the corresponding response of humidity. Using unstandardized regression slopes, we find that mesoscale ascent partially offsets entrainment-driven isotopic depletion ~~with an efficiency of 1.19, meaning 1 mm~~with approximately 0.7 mm s⁻¹ of ~~vertical velocity more than cancels~~upward motion required to counteract the isotopic effect of ~~1 mm~~mm s⁻¹ of entrainment. The strongest correlations between vertical velocity and both ~~δD~~ δD ($r \approx 0.52$) and mixing ratio ($r \approx 0.39$) occur within ± 200 m of the subcloud layer ~~(SCL) top. A top, indicating where mesoscale circulations most directly influence near-surface composition. A steady-state~~flux-form mixed-layer model reproduces these asymmetric responses the observed asymmetric responses of δD and humidity, providing mechanistic ~~understanding of insight into~~how mesoscale circulations fundamentally modulate boundary layer moisture processes ~~reorganize moisture pathways without producing commensurate changes in total~~water vapor.

1 Introduction

Shallow cumulus clouds in the trade-wind regions are ubiquitous and exert a cooling influence on the climate, but their response to warming remains ~~highly~~uncertain (Bony and Dufresne, 2005). These low clouds have long been recognized as a leading source of spread in climate model projections of global warming (Sherwood et al., 2014). Many climate models predict a ~~positive~~positive trade cumulus cloud feedback governed by reductions in cloud fraction near cloud base. In particular, higher-sensitivity models tend to produce more efficient entrainment of dry air from aloft, which depletes low-level humidity and erodes cloud cover (Sherwood et al., 2014). This hypothesized mixing–desiccation mechanism posits that vigorous shallow convective mixing dries the lower troposphere and dissipates clouds, thereby amplifying surface warming as a positive low-cloud feedback.

Recent observations, however, challenge this ~~simple~~simple picture. In early 2020, the EUREC⁴A field campaign (Elucidating the ~~Role of Clouds–Circulation Coupling in Climate~~) was conducted near Barbados with a ~~comprehensive~~comprehensive network of research

aircraft, ships, and ground stations to study trade-wind cumulus and their environment (Bony et al., 2017; Stevens et al., 2021). Analyses of EUREC⁴A data revealed ~~ubiquitous~~-shallow mesoscale circulations on scales of roughly 100–200 km that organize convection and concentrate moisture in the trades (George et al., 2023). Consistent with this, periods of stronger mesoscale ascent did not lead to a drier subcloud layer (SCL) or reduced cloudiness, contrary to the mixing–desiccation expectation (Vogel et al., 2022). Instead, the observations suggest that mesoscale cloud–circulation coupling can maintain humidity, implying that factors beyond one-dimensional entrainment, such as horizontal convergence and large-scale vertical motion, significantly influence low-level moisture and cloud cover. Nevertheless, disentangling the contributions of these processes, for example separating the effects of shallow convective detrainment from those of large-scale subsidence, remains challenging with conventional measurements alone. Standard thermodynamic observations cannot easily attribute moisture variability to specific physical processes, leaving an important gap in process-level understanding of the trade cumulus regime.

Stable water isotopologues offer a way to fill this gap. The ratios of heavy to light water isotopologues in vapor, such as $\text{H}_2^{18}\text{O}/\text{H}_2^{16}\text{O}$ or $\text{HDO}/\text{H}_2\text{O}$, commonly reported as $\delta^{18}\text{O}$ and δD , are sensitive to the cumulative phase-change history of an air mass (Galewsky et al., 2016). Condensation and rainout preferentially remove heavy isotopes, so air that has undergone extensive convective uplift and precipitation is left isotopically depleted in heavy molecules relative to ocean water. In contrast, addition of moisture by evaporation from the warm ocean surface, or by mixing with unsaturated air from below, enriches the vapor in heavy isotopes. Thus, water vapor isotopic measurements can serve as tracers of moisture origin and transport. They enable us to distinguish between air masses that have experienced different water-cycle processes and to test hypotheses about what controls an air mass’s humidity and cloud-forming potential. Past studies have demonstrated that isotopic variations can be used to identify moisture sources and quantify mixing between atmospheric layers, processes that are largely indistinguishable in bulk humidity alone (Risi et al., 2019; Galewsky et al., 2016).

~~Motivated by this~~, EUREC⁴A included a coordinated initiative (EUREC⁴A-iso) to deploy an extensive network of water vapor isotope analyzers across multiple platforms (Bailey et al., 2023). Seven laser-based instruments, sampling at up to 0.5 Hz, were operated on two research aircraft, three ships, and at the Barbados Cloud Observatory during the campaign. This data set provides the high-resolution, multi-platform coverage needed to close regional moisture budgets and ~~rigorously~~-evaluate model simulations of moist processes. Here, we ~~leverage~~use the EUREC⁴A water vapor isotopic measurements from the R/V Meteor to bridge the gap between documented mesoscale circulation effects and their impacts on the marine boundary layer moisture budget. Specifically, we use the stable isotope signatures to directly track shallow convective mixing and its influence on lower-tropospheric moisture in the trade-wind regime.

2 Data

~~EUREC4A comprised roughly~~ EUREC⁴A comprised about 5 weeks of measurements in the downstream winter trades of the North Atlantic, eastward and southeastward of Barbados. The campaign deployed an extensive observational network to characterize processes operating across scales from micrometers to hundreds of kilometers. The measurements included 2500 atmospheric soundings to quantify mesoscale and larger-scale ~~circulations~~atmospheric properties, approximately 400

flight hours by four research aircraft, operations from four research vessels, and continuous observations from a ground-based cloud observatory. Additional platforms included autonomous systems that collected nearly 10,000 upper-ocean profiles, continuous atmospheric boundary layer measurements, air-sea interface observations, water vapor isotopologue measurements across multiple platforms, coordinated satellite observations, and support from high-resolution numerical weather and climate models.

2.1 Upper Air Data

The dropsonde measurements were conducted using two research aircraft: the High Altitude and Long Range Research Aircraft (HALO) dropsonde measurements were conducted as a core part of the EUREC4A field campaign (Konow et al., 2021) and the NOAA WP-3D Orion (P-3) (Pincus et al., 2021). The primary scientific motivation for these measurements was to characterize the mesoscale meteorological area-averaged kinematic environment of trade-wind cumulus cloud fields and to quantify area-averaged vertical motion in the marine boundary layer. The cornerstone of the HALO measurement strategy was the EUREC4A circle EUREC⁴A circle (Figure 1), a standardized circular flight pattern designed to enable accurate estimates of mesoscale circulation properties including divergence, vorticity, and vertical velocity. This approach, adapted from Lenschow et al. (1999, 2007) and Bony and Stevens (2019), exploits the assumption that atmospheric variations at the mesoscale can be approximated as linear in horizontal space over the scale of a single aircraft circle.

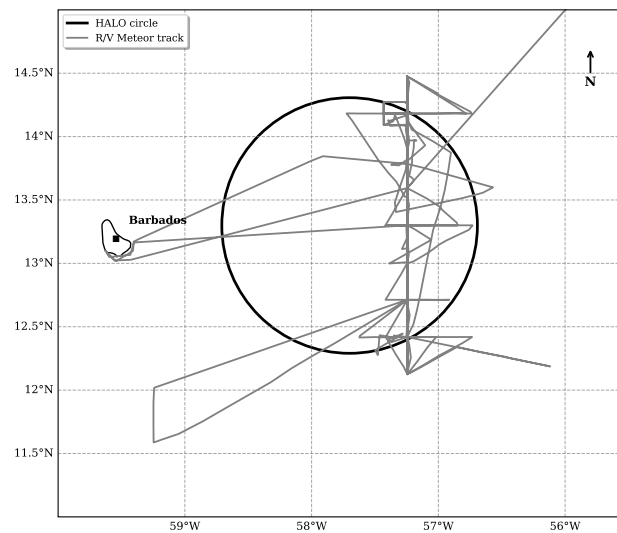


Figure 1. Map of the EUREC4A-EUREC⁴A study area showing a representative HALO-EUREC⁴A circle pattern and the R/V Meteor ship track. The circle (black) represents one of the 222 km diameter flight patterns used for dropsonde deployment to measure mesoscale circulation. The ship track (gray) shows the path of R/V Meteor during the January–February 2020 field campaign.

The EUREC4A circle EUREC⁴A circle was centered at 13.30°N, 57.72°W with a diameter of approximately 222 km. Each circle flight pattern deployed 12 dropsondes at regular intervals around the circumference, with launches separated by

approximately 5 minutes corresponding to the aircraft’s 60-minute circuit time. This systematic sampling enables estimation of horizontal gradients through regression analysis, from which mesoscale circulation properties can be derived.

A total of ~~70 EUREC4A circles were flown by HALO~~ 85 EUREC⁴A circles were flown during the campaign (71 by HALO and 14 by the P-3), providing unbiased sampling across meteorological conditions. HALO All flights operated from Bridgetown, Barbados, with HALO operating at altitudes between 10.0–10.5 km, while the P-3 typically flew at lower altitudes near 7.5 km as part of the ATOMIC component of the campaign (Pincus et al., 2021). A total of ~~895–1216~~ Vaisala RD-41 dropsondes were launched (896 from HALO and 320 from the P-3), each containing pressure, temperature, and humidity sensors sampling at 2 Hz, along with GPS receivers providing wind measurements at 4 Hz. The measurements are archived in the JOANNE dataset (George et al., 2021), from which we use the Level 4 circle-averaged products containing mesoscale diagnostics derived through regression analysis of the 12-sonde circle patterns. These products include horizontal gradients of atmospheric variables and derived quantities such as divergence, vorticity, horizontal divergence of wind velocity, and vertical velocity, with associated uncertainty estimates from the regression fitting.

The subcloud layer height h used here was first presented in Vogel et al. (2022) and is determined using a temperature-based threshold method (Albright et al., 2022). Specifically, h is defined as the height where the virtual potential temperature θ_v first exceeds its density-weighted mean value (computed from 100 m up to h) by a fixed threshold $\epsilon = 0.2$ K (Vogel et al., 2022). This approach follows established methodology for identifying the top of the well-mixed subcloud layer (Touzé-Peiffer et al., 2022). The method accounts for the finite thickness of the transition layer separating the mixed layer from the cloud layer above (Albright et al., 2022). This transition layer, approximately 150 m thick, complicates the application of classical mixed-layer theory which assumes an infinitesimally thin inversion.

The entrainment rate E is computed using a modified flux-jump model (Albright et al., 2022; Vogel et al., 2022) that extends the classical approach of Lilly (1968) and Stull (1976). The entrainment rate represents the deepening of h due to small-scale mixing at the subcloud layer top. This approach differs from the zero-order jump models that assume instantaneous transitions (Lilly, 1968) by accounting for the finite depth of the entrainment zone, providing a more realistic representation of the actual atmospheric structure observed during ~~EUREC4A~~ EUREC⁴A. Note that throughout this study, E refers only to entrainment from the cloudy layer (CL) into the subcloud layer (SCL). It does not include exchange between the CL and the free troposphere (FT). Here, E represents a diagnostically inferred entrainment tendency at the cloud–subcloud interface; negative values indicate periods of interface descent or weak detrainment rather than physically negative turbulent entrainment. Across the matched circles, the average entrainment rate, $E = 18.8 \pm 6.9$ mm s⁻¹ and the average subcloud layer height is $h = 0.69 \pm 0.10$ km.

105 2.2 Isotopic and Surface Data

Water vapor isotope measurements aboard the R/V Meteor were obtained using a Picarro L2130-i cavity ring-down spectrometer (CRDS) operating at 1 Hz resolution from January 18 to February 22, 2020. The analyzer was housed in the Air-Chemistry Laboratory at ~ 20.3 m above sea level, sampling ambient air through a 5 m long, 4.6 mm ID PTFE inlet line heated to 45°C and insulated with polyethylene foam. The inlet was housed in a downward-facing funnel to minimize contamination from

110 rainwater and sea spray, and included a 0.2 μm PTFE aerosol filter. Flow was controlled by the CRDS system at approximately 0.03 slpm, resulting in a time delay of >2 minutes from intake to analyzer. Daily calibration checks were performed using four liquid water standards spanning $\delta^{18}\text{O}$ values from -20.97 to -2.79‰ and δD values from -158.13 to -13.12‰ , delivered in gas phase using a Picarro Standards Delivery Module. Prior to normalization, isotopic observations were corrected for small humidity-dependent biases of up to 0.24‰ in $\delta^{18}\text{O}$ and 0.36‰ in δD . Total uncertainties were estimated at 0.29‰ for $\delta^{18}\text{O}$ and 1.24‰ for δD by summing in quadrature the uncertainties associated with liquid standards, humidity-dependence correction, calibration measurement precision, and temporal drift over the campaign. Further details on the isotopic data collection program can be found in Bailey et al. (2023).

Near-surface relative humidity data were obtained from temperature and dew point measurements made at 29 m above the sea surface on the Meteor's mast. SST was measured at 2.3 m depth with matching port and starboard sensors.

120 3 Results

Figure 2 presents the full time series of surface water vapor measurements, relative humidity (RH) and sea surface temperature (SST) measured from the R/V *Meteor* during ~~EUREC4A~~EUREC⁴A. The dataset exhibits ~~remarkably~~relatively low variability across all measured parameters, reflecting the stable trade wind conditions that characterized the campaign period. Water vapor mixing ratios varied with a standard deviation of ~~only~~ 0.832 g kg^{-1} around a mean of 15.1 g kg^{-1} , while δD showed a standard deviation of 1.94‰ around a mean of -70.6‰ . Surface meteorological ~~conditions were similarly constrained~~variability was also limited, with relative humidity varying by 4.6% around a mean of 71.6% and sea surface temperatures showing ~~minimal~~little variation (standard deviation 0.23°C) around 27.3°C . The measurement uncertainty for ~~6-hour~~2-hour averaged isotope data (1.24‰ for δD) represents approximately 65% of the observed natural variability, ~~constraining~~limiting our ability to detect weak atmospheric signals. Consequently, our analysis focuses on the strongest and most robust correlations that exceed this measurement noise threshold.

Figure 3 shows the vertical correlation structure between ~~HALO-derived~~dropsonde-derived vertical velocity and surface isotopic composition (δD) and mixing ratio as a function of altitude relative to the top of the subcloud layer. Both δD (solid line) and mixing ratio (dashed line) exhibit their strongest correlations just below this boundary. The isotopic signal shows peak correlation ($r \approx 0.52$) about 100 meters below the top of the SCL, while humidity correlations reach maximum strength ($r \approx 0.39$) about 100 meters lower within the SCL.

~~The enhanced correlations within this relatively narrow altitude range show that vertical velocity exerts its primary influence on surface humidity through processes operating near the top of the subcloud layer.~~

Figure 4 shows (a) entrainment rate E (light blue) and vertical velocity W from 100 m below the top of the SCL (dark blue), both in mm s^{-1} ; (b) surface $\delta\delta\text{D}$ in ‰ ; and (c) water vapor mixing ratio in g kg^{-1} . Each point represents a ~~6-hour~~2-hour average centered on a HALO/P3 circle time. The time series shows coherent variability across all of these parameters. Periods of enhanced entrainment (positive E values) consistently coincide with more negative δD and lower mixing ratio, as seen most clearly around January 26. Conversely, periods of weak entrainment or stronger mesoscale ascent (negative E ,

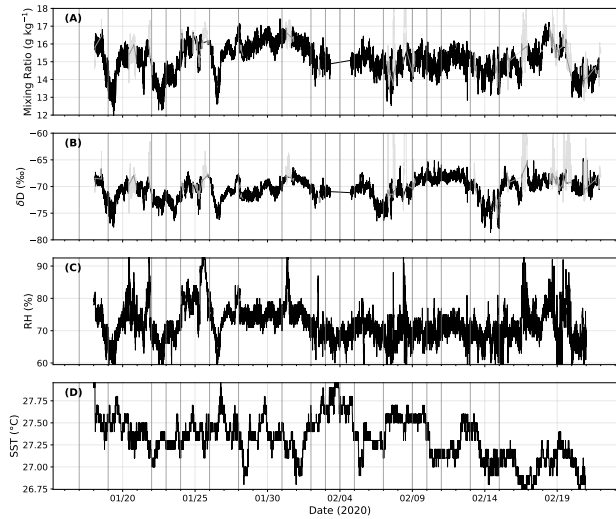


Figure 2. Time series of surface measurements from R/V *Meteor* during [EUREC4A/EUREC4A](#), January 18–February 22, 2020. (A) Water vapor mixing ratio from Picarro L2130-i cavity ring-down spectrometer at 1-minute resolution. (B) Deuterium isotope ratio (δD) from the same instrument. (C) Relative humidity from shipboard meteorological sensors. (D) Sea surface temperature. Black lines indicate quality-controlled data; pale gray points show measurements flagged during quality control. Gray vertical lines mark days with HALO/P3 aircraft circle flights from the JOANNE dropsonde dataset.

positive W) correspond to less negative δD and higher mixing ratios, evident around January 24 and February 1. Entrainment brings dry, isotopically depleted air from above the SCL into the surface layer, reducing humidity and driving δD toward more negative values ([and overwhelming any potential increase in surface evaporation due to associated winds](#)). Periods of reduced entrainment or mesoscale upward motion allow the boundary layer to maintain higher humidity and preserve the enriched isotopic signatures characteristic of ocean evaporation.

This [structure](#) is further illustrated in Figure 5, which shows the relationship between vertical velocity W (x-axis) and entrainment rate E (y-axis), with points colored by surface δD values and sized according to water vapor mixing ratio. The scatter plot [shows-reveals](#) a systematic organization of boundary layer states across the E - W parameter space. Points in the [upper-left](#) quadrant (negative W , high E) represent conditions of strong entrainment combined with [downdrafts, mesoscale downdrafts and are](#) characterized by more negative δD values and low mixing ratios. Points toward the lower right (positive W , low E) indicate periods of [weaker entrainment and](#) mesoscale ascent, which are associated with [higher \$\delta D\$ values and higher mixing ratios](#). This [figure demonstrates that \$E\$ and \$W\$ are not entirely less negative \$\delta D\$ values and modestly higher humidity](#).

[A linear regression across all matched circles \(\$n = 56\$ \) yields](#)

$$E = -0.25(\pm 0.24)W + 18.6, \quad (1)$$

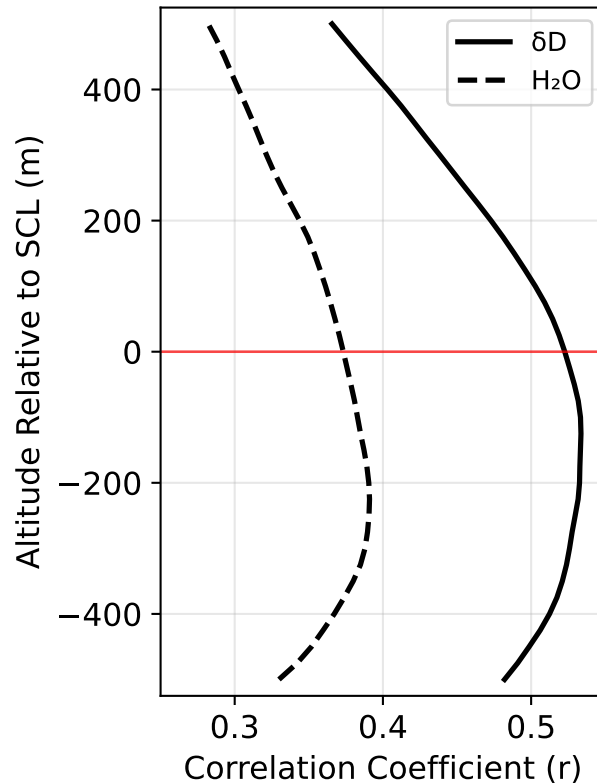


Figure 3. Vertical velocity correlation profiles with isotopic composition and humidity near subcloud layer height. Correlation coefficients between vertical velocity (W) and water vapor δD (solid black line) and water vapor mixing ratio (dashed black line) are shown as functions of altitude relative to the top of the subcloud layer (SCL, red horizontal line at 0 m). The analysis spans ± 500 m around the top of the SCL, which is defined as the height where virtual potential temperature first exceeds its density-weighted mean from 100 m by 0.2 K. Both variables show peak correlations within the subcloud layer, with δD exhibiting stronger coupling to vertical motion than humidity.

with a statistically significant negative slope ($p = 0.044$, 95% confidence interval $[-0.49, -0.01]$), indicating that entrainment and vertical velocity are weakly but systematically anticorrelated. Although this relationship exhibits substantial scatter, it demonstrates that E and W are not independent but instead define span a continuum of boundary layer mixing states.

The color gradient from dark (depleted) to light (enriched) δD values follows a clear diagonal pattern from high E , negative W conditions toward low E , positive W conditions. Similarly, marker

Consistent with this organization, the δD color gradient transitions from more depleted values under high- E , negative- W conditions toward more enriched values under low- E , positive- W conditions. Marker sizes increase along this same trajectory, indicating that periods of reduced entrainment and upward motion coincide with both mesoscale ascent coincide with isotopic enrichment and enhanced humidity.

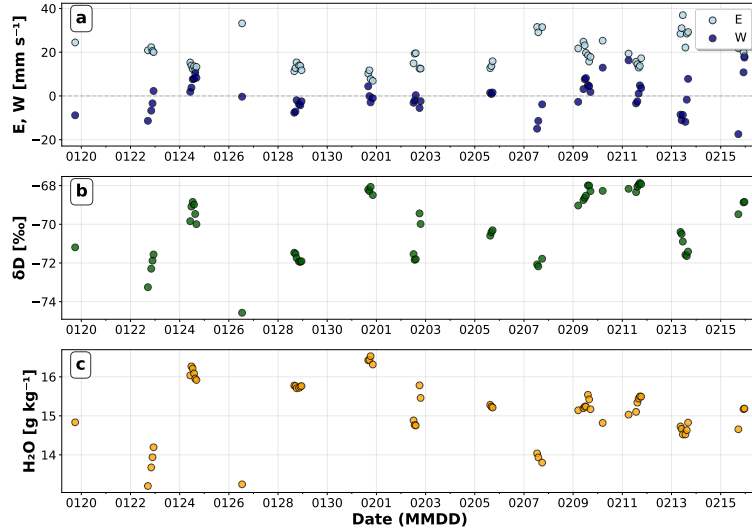


Figure 4. Time series of atmospheric variables during the [EUREC4A-EUREC4A](#) campaign. (a) Entrainment rate E (light blue) and mesoscale vertical velocity W from 100 m below the top of the SCL (dark blue) in mm s^{-1} , showing the competing effects of horizontal dry air mixing and convective vertical motion. The dashed gray line indicates zero. (b) Surface boundary layer δD in ‰, measured by ship-based Picarro analyzer. (c) Water vapor mixing ratio H_2O in g kg^{-1} from matched [HALO-Picarro-HALO/P3-Picarro](#) observations. All data points represent [6-hour-2-hour](#) averaged values spatially matched within HALO/P3 flight circles. The time axis shows dates in MMDD format during January-February 2020. Data demonstrate the temporal evolution of entrainment-convection competition and its effects on boundary layer moisture and isotope signatures.

A more quantitative understanding of these relations is illustrated in Figs. 6 and 7. Figure 6 shows the joint dependence of isotopic composition and humidity on both entrainment and vertical velocity. Panel (A) shows δD values across the E - W parameter space, with contour lines representing predictions from a joint linear regression model that includes both E and W as predictors. The isotopic field exhibits a systematic gradient from depleted values ($\delta D \approx -73\text{‰}$) at high entrainment rates and negative vertical velocities to enriched values ($\delta D \approx -68\text{‰}$) at low entrainment and positive vertical velocities. Panel (B) shows the corresponding humidity field, where water vapor mixing ratios decrease from approximately 16.5 g kg^{-1} at low ~~E and high W~~ E and high W to 13.5 g kg^{-1} at high ~~E and low W~~ E and low W . To quantify these relationships, we performed a joint multilinear regression for both variables. The regression for δD yields $\delta D = -0.071E + 0.100W - 68.74$ ($R^2 = 0.357$), where both predictors are statistically significant at the 5% level ($p \approx 0.013$ for E and $p \approx 0.00027$ for W), with a residual mean absolute error (MAE) of 1.15‰ and an RMSE of 1.33‰ . For specific humidity, the regression yields $H_2O = -0.083E + 0.019W + 16.72$ ($R^2 = 0.633$), with coefficients that are also significant ($p \approx 2.5 \times 10^{-11}$ for E and $p \approx 0.040$ for W) and a residual MAE of 0.365 g kg^{-1} and RMSE of 0.472 g kg^{-1} . These results quantify the “diagonal” structure seen in the parameter space, demonstrating that both predictors are statistically significant, with a moderate fit for δD

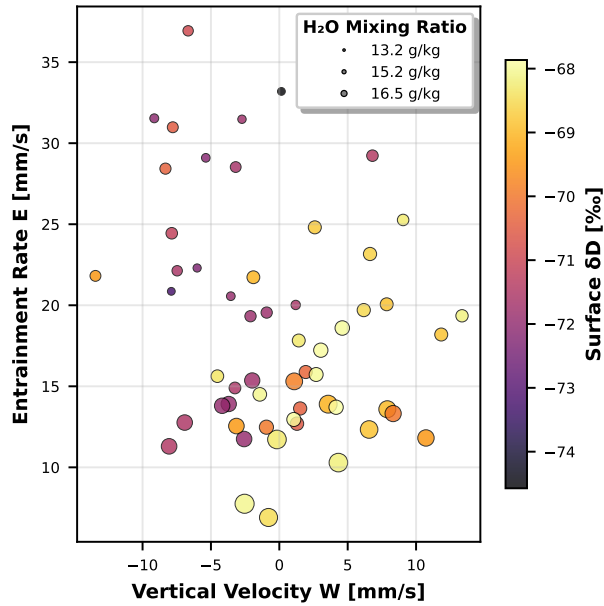


Figure 5. Relationships between vertical velocity (W), entrainment rate (E), water vapor mixing ratio, and water vapor δD during EUREC4A/EUREC4A. Scatter plot shows W extracted at optimal altitude of maximum correlation from Figure 4 (567.7 m above the sea surface) versus entrainment rate E , with circle size proportional to water vapor mixing ratio (H_2O) and color representing surface δD . Data points represent individual dropsonde circles matched with ship-based isotope measurements.

180 and a stronger fit for H_2O . The orientation of the contours in both panels shows further confirms that δD is more sensitive to W than the total mixing ratio, which is more sensitive to entrainment.

In interpreting these results, we note that E and W are not independent predictors; in our dataset, they exhibit a modest negative correlation ($r \approx -0.27$). However, the joint multilinear regression framework used here specifically accounts for this covariance. The reported MLR coefficients represent partial slopes, quantifying the independent impact of each variable while holding the other constant. Consequently, the distinct sensitivities observed for δD and humidity are robust signatures of the physical processes driving each variable, rather than artifacts of the correlation between entrainment and vertical motion.

Figure 7 further quantifies the counteraction effect of W on E mesoscale vertical velocity (W) on entrainment (E) through residual analysis. This approach first removes the linear effect of entrainment alone, then quantifies examines how vertical velocity correlates with the remaining variance. The δD Using the full dataset ($n = 56$), the standardized regression coefficients for δD are $\beta_E = -0.49$ and $\beta_W = +0.74$. For humidity, the standardized coefficients are $\beta_E = -0.57$ and $\beta_W = +0.14$. These coefficients are obtained from the joint regression and do not assume independence between E and W .

The δD residuals (Panel A) show A) exhibit a strong positive correlation with W ($r = 0.464$), indicating that upward motion systematically counteracts entrainment-driven depletion. The counteraction efficiency is defined isotopic depletion. We define a counteraction efficiency metric as the ratio of the W regression slope to the E regression slope and

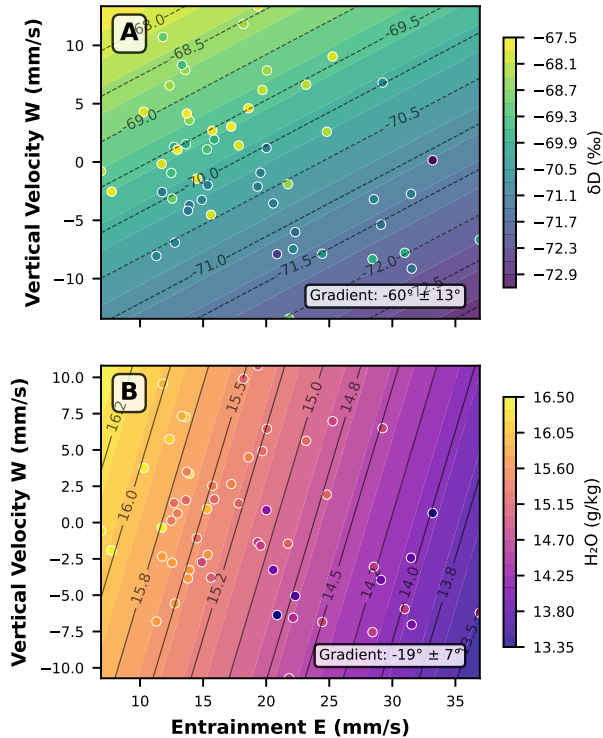


Figure 6. Joint entrainment-vertical velocity dependencies in isotopic composition and humidity fields. (A) Contour plot showing water vapor δD as a function of entrainment rate E and vertical velocity W , with observations overlaid as colored points. Contour lines represent predictions from the joint E - W regression model. (B) Water vapor mixing ratio (H_2O) dependencies on the same E - W parameter space, using a different color scheme to distinguish variables.

195 reaches 1.19 for δD , meaning that 1 absolute values of the standardized regression coefficients,

$$\eta = \left| \frac{\beta_W}{\beta_E} \right|, \quad (2)$$

which quantifies the relative statistical influence of mesoscale ascent and entrainment in units of standard deviations. For δD , this yields $\eta_{\delta D} \approx 1.5$, whereas for humidity the corresponding value is much smaller, $\eta_q \approx 0.25$.

200 Because this metric is based on standardized coefficients, it does not represent cancellation in physical units (mm s^{-1}), but instead compares the sensitivity of each variable to variability in the two predictors. Physical cancellation in mm s^{-1} can instead be assessed using the unstandardized regression slopes. From the fitted relationship

$$\delta D = -0.071 E + 0.100 W - 68.74, \quad (3)$$

we find that approximately 0.7 mm s^{-1} of upward motion counteracts the isotopic effect of 1.19 mesoscale ascent is required to offset the isotopic impact of 1 mm s^{-1} of entrainment.

205 For water vapor (Panel B), the counteraction is weaker, with $r = 0.270$ and an efficiency of 0.30. Mesoscale vertical velocities exerts a much stronger control on isotopic composition than on humidity itself. The efficiency greater than unity for δD

The counteraction efficiency for δD indicates that mesoscale processes dominate over entrainment in determining surface isotopic signatures, while the much exert a stronger relative influence on isotopic variability than entrainment alone, whereas the lower efficiency for humidity reflects the more equitable relationship between vertical motion and entrainment in setting the comparatively weak role of vertical motion in setting boundary-layer water vapor concentrations in the boundary layer. While these correlations, Although these relationships exceed the noise threshold identified earlier, we note that the measurement uncertainty represents measurement uncertainty constitutes a large fraction of the observed δD variance. Thus δD variance. As a result, the precise values of the regression slopes and efficiencies should be interpreted with caution cautiously, even though the qualitative pattern of a stronger isotopic than humidity response contrast between isotopic and humidity responses is robust.

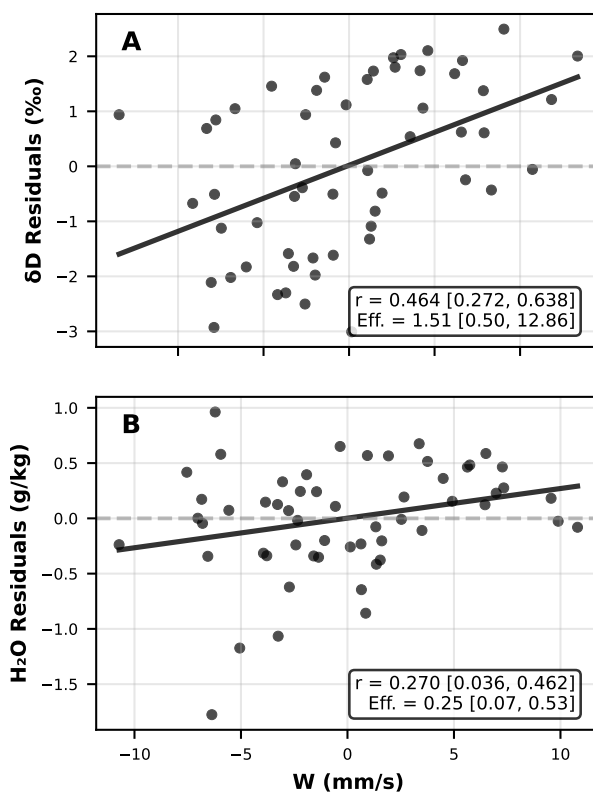


Figure 7. Residual analysis of vertical velocity counteraction effects on isotopic composition and humidity. (A) ΔD residuals after removing entrainment-only effects plotted against vertical velocity W at optimal altitude. Points show individual HALO/P3 circle observations, with the regression line indicating the pure counteraction effect of W . The correlation coefficient (r) and counteraction efficiency (Eff.) quantify how effectively vertical motion counteracts entrainment-driven isotopic depletion. (B) Water vapor mixing ratio (H_2O) residuals after removing entrainment-only effects plotted against vertical velocity W .

215 These results demonstrate show that mesoscale circulations significantly modulate the entrainment-driven changes in boundary layer humidity and composition, consistent with the findings of Vogel et al. (2022) and George et al. (2023). The isotopic measurements provide quantitative constraints on the relative importance of these competing processes, with mesoscale vertical motions capable of fully offsetting or even reversing entrainment effects on boundary layer moisture characteristics δD .

3.1 Mixed-Layer Flux-Form Mixed-Layer Model ~~To better understand the processes~~

220 To identify the physical mechanisms responsible for the asymmetric responses of δD δD and q to entrainment and mesoscale vertical motion, we implemented a steady-state, we applied the flux-form mixed-layer model (Appendix A). The model represents the boundary layer as a single, well-mixed slab in which water vapor and its isotopic composition are described in Appendix A. Unlike simpler mixing definitions that treat the subcloud layer (SCL) as a passive reservoir, this model explicitly resolves the competing isotopic fluxes driven by surface evaporation, entrainment mixing, and active hydrometeor exchange.

225 The model's moisture budget is determined by the balance between two primary processes: surface evaporation, turbulent entrainment which moistens and isotopically enriches the boundary layer, and entrainment of air from the cloudy layer, and large-scale vertical motions. Surface evaporation is parameterized using which dries and isotopically depletes it. We formulate the surface flux using a physically consistent Craig-Gordon theory, and entrainment is prescribed as an independent flux of approximation that accounts for the cancellation of humidity singularities in the mass and isotope budgets (see Appendix
230 A), ensuring that the model respects the mass and isotopes from the overlying air. Mesoscale vertical velocity influences the model both directly, by modulating the net mass budget of the mixed layer, and indirectly, by altering the effective entrainment rate. This simple framework captures the observed contrast in sensitivity, with δD responding much more strongly than q to variations in mesoscale vertical motion, thereby providing a mechanistic interpretation of the asymmetries seen in the observations. balance constraints of the system.

235 Figure ?? shows the sensitivity of modeled boundary layer humidity (q) and isotopic composition (δD) to mesoscale vertical velocity W , expressed in standardized units to facilitate comparison. For each variable, anomalies are computed relative to the model state at $W = 0$ and then normalized by the corresponding standard deviation from the observational campaign ($\sigma_q = 0.832 \text{ g kg}^{-1}$, $\sigma_{\delta D} = 1.94 \text{ ‰}$). Expressing the results in these σ units allows a direct comparison of the relative strength of However, standard mixing dynamics alone cannot reproduce the observed slope separation between δD and humidity. In
240 a "passive" mixing regime, where the SCL interacts only with the W -induced changes in ocean surface and the dry free troposphere, isotopic composition and humidity are tightly coupled, resulting in δD and q and δD despite their different physical units and variances. A slope of unity in these units would correspond to a change equal to one observed standard deviation per 1 cm s^{-1} change in W . contours that are nearly parallel. To capture the observed orthogonality (Fig. 8), the model must account for the active processing of water vapor by liquid water within the trade-wind layer.

245 Sensitivity of boundary layer mixing ratio (q) and isotopic composition (δD) to mesoscale vertical velocity from the flux-form mixed-layer model. Curves show anomalies of δD (solid) and q (dashed) expressed in observational σ units versus vertical velocity W (cm s^{-1}), at fixed entrainment $E = 20, \text{ mm s}^{-1}$.

The curves in Figure ?? exhibit a clear asymmetry in the modeled responses. For $W > 0$ (mesoscale ascent), both q and δD increase, while for $W < 0$ (descent) they decrease. However, the magnitude of the response in δD is much larger: the model yields a linear sensitivity of about $3.72 \sigma_{\delta D}$ per cm s^{-1} , compared to only $0.49 \sigma_q$ per cm s^{-1} for q , a ratio of roughly 7.5. This difference reflects the fact that δD is sensitive not only to changes in total water mass but also to shifts in the isotopic composition of the entrained air. In the model, mesoscale ascent reduces the relative contribution of isotopically depleted CL air, driving δD upward, while mesoscale descent enhances the entrainment influence and lowers δD . Because q is controlled solely by the net mass fluxes, its fractional changes are smaller.

This modeled behavior parallels the observational results: in both, We therefore introduce a hydrometeor exchange mechanism that represents the interaction between subcloud vapor and falling rain or drizzle droplets. This process is physically justified by the ubiquity of warm rain in the trade-wind regime; EUREC⁴A observations confirm that rain evaporation is a frequent and significant contributor to the subcloud moisture budget, often manifesting as cold pools (Touzé-Peiffer et al., 2022; Radtke et al., 2022). Previous modeling studies of trade cumulus have similarly established that rain evaporation is a critical term for closing the isotopic budget, as falling droplets transport heavy isotopes from the cloud layer back into the subcloud environment (Risi et al., 2020).

In our model, this exchange is parameterized as a relaxation toward an enriched hydrometeor equilibrium, with an efficiency that scales with mesoscale vertical velocity (W). Physically, this dependency reflects the dynamical nature of the cloud field: mesoscale ascent organizes convection and increases cloud fraction (George et al., 2023), thereby generating the precipitation flux necessary to drive isotopic exchange. During periods of ascent, this “recharging” mechanism counteracts the depletion caused by entrainment, effectively buffering the isotopic composition responds much more strongly to mesoscale vertical motion than does humidity, and of the boundary layer even as entrainment continues to regulate the bulk humidity.

Figure 8 presents the modeled equilibrium state for humidity (dashed blue contours) and δD (solid black contours) across the entrainment-vertical velocity (E - W) phase space. The model successfully reproduces the nearly orthogonal structure observed in the campaign data (compare to Figure 6). The modeled humidity contours are steep (slope $\approx 77^\circ$), indicating that q_{BL} is primarily controlled by the entrainment rate E and is relatively insensitive to W . In contrast, the sign of the response is consistent with the balance between surface evaporation and entrainment from the CL. The σ -unit scaling underscores that the stronger isotope response is not an artifact of measurement units, but reflects a genuinely greater fraction of the observed variability being explained by modeled δD contours are much flatter (slope $\approx 35^\circ$), indicating an important sensitivity to vertical velocity. This successful reproduction of the E - W in δD than in q . This asymmetry emerges naturally from the model physics, without requiring any ad hoc tuning, and provides a simple mechanistic explanation for the patterns seen in the data phase space provides evidence that the trade-wind boundary layer cannot be treated as a simple two-component mixing system; rather, its composition is actively shaped by phase-change physics modulated by mesoscale circulations.

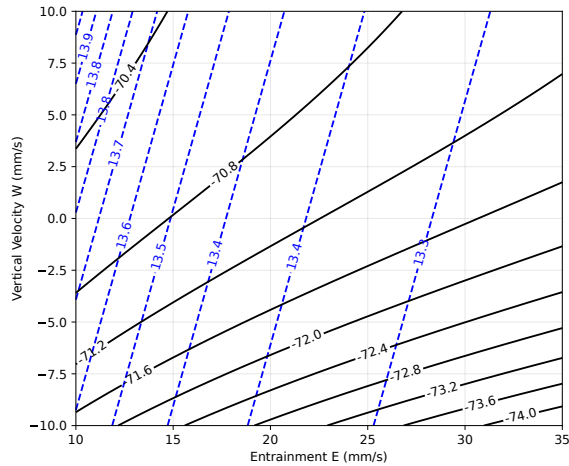


Figure 8. Equilibrium solution of the strictly consistent flux-form mixed-layer model (v23) across the entrainment (E) and vertical velocity (W) parameter space. Dashed blue lines show specific humidity (q_{BL}), which is dominated by entrainment (steep contours). Solid black lines show isotopic composition (δD), which is strongly modulated by vertical velocity (flatter contours). The divergence of these slopes (approx. 77° vs. 35°) reproduces the first-order effects observed in the EUREC⁴A data, showing how active isotopic exchange during ascent is required to explain the observations.

4 Discussion

280 Our analysis shows that mesoscale vertical motions in the ~~trades strongly modulate~~ trade-wind regime modulate the marine boundary layer ~~moisture by counteracting through a partial counteraction of~~ entrainment-driven drying. Water vapor isotopologues reveal this ~~process with much modulation with~~ greater sensitivity than humidity alone, ~~highlighting yielding~~ an asymmetric response ~~in which water vapor: δD responds much more strongly to changes in mesoscale vertical velocities than varies more strongly with mesoscale vertical velocity than does~~ the total mixing ratio. A flux-form mixed-layer model reproduces

285 this behavior ~~-, demonstrating that and indicates that, under the observed conditions, δD responds about 7.5 six~~ times more strongly than humidity to mesoscale vertical motion. ~~These findings underscore the critical role of mesoscale circulations in shaping humidity and isotopic composition in the trade-wind regime. Recall that throughout~~ Together, these results show that mesoscale circulations reorganize boundary layer moisture in ways that are weakly expressed in humidity but strongly expressed in isotopic composition.

290 Throughout this study, E refers ~~only exclusively~~ to entrainment from the cloudy layer (CL) into the subcloud layer (SCL) and ~~it~~ does not include exchange between the CL and the free troposphere (FT). Negative values of E are interpreted as reflecting reduced or reversed apparent entrainment tendencies associated with mesoscale subsidence or interface lowering, rather than literal negative turbulent entrainment fluxes.

Our findings can be placed in the context of the analytical and LES-based framework of Risi et al. (2020). In their simulations, the primary mechanism depleting near-surface vapor was the export of isotopically enriched air by convective updrafts, with downdrafts and rain evaporation providing additional contributions. They argued that the classical amount effect emerges because stronger large-scale ascent steepens vertical isotopic gradients, thereby enhancing the efficiency of updrafts and downdrafts in depleting the subcloud layer. In contrast, our EUREC⁴A analysis highlights the sensitivity of δD to mesoscale vertical motions within the trade inversion layer: shallow mesoscale updrafts counteract entrainment-driven import of depleted cloudy-layer air and thus enrich the subcloud layer, while mesoscale downdrafts enhance the isotopic depletion. Both perspectives underscore the role of vertical motions in setting near-surface isotopic composition, but at different scales and regimes: large-scale ascent and deep convection in Risi et al. (2020), versus shallow mesoscale overturning circulations within the trades in this study. Together, these results suggest that the isotopic composition of boundary layer vapor is highly sensitive to the scale and vertical structure of vertical motions, which can act either to enrich or to deplete depending on the dynamical context.

305

4.1 Connection to mesoscale overturning circulations and mixing-desiccation processes

~~Our results provide mechanistic closure.~~ These findings provide observational and mechanistic context for the shallow mesoscale overturning circulations (SMOCs) identified by George et al. (2023) and the counteraction mechanism proposed by Vogel et al. (2022). ~~Vogel et al. (2022) refuted the mixing-desiccation demonstrated that mesoscale vertical motions counteract entrainment-driven drying, refuting the mixing-desiccation hypothesis of Sherwood et al. (2014) by showing that mesoscale vertical motions and entrainment contribute comparably to subcloud layer budgets, but with opposite signs for their impact on humidity. They concluded that stronger mixing does not desiccate cloud base because mesoscale circulations counteract the drying expected from entrainment. Meanwhile, George et al. (2023) provided the first necessarily lead to cloud-base desiccation. George et al. (2023) provided~~ direct observational evidence of SMOCs ~~in the trade wind layer, showing robust dipoles in divergence, documenting robust divergence dipoles~~ between the subcloud and cloud layers, ~~spatial scales of ~ 100 – 200 km, and ubiquitous coverage ($\sim 58\%$ of a $10^\circ \times 10^\circ$ domain). They demonstrated that SMOCs amplify moisture variance at cloud base, with strong anti-correlation between subcloud divergence anomalies and q at cloud base (Pearson $r \approx -0.67$), and proposed that and showing that convergence branches reduce entrainment drying efficiency in ascending regions, driving bottom-heavy moisture variance efficiency and amplify moisture variance near cloud base.~~

By exploiting water vapor isotopologues, we bridge these complementary findings and provide a missing process-level attribution. Our δD measurements serve as direct tracers of source contributions, showing that mesoscale ascent maintains enriched isotopic signatures characteristic of oceanic evaporation, while entrainment introduces isotopically depleted air from the CL. This renders the qualitative compensation mechanisms of both studies directly observable in boundary layer composition. Quantitatively, we show that mesoscale ascent offsets entrainment-driven depletion of δD with an efficiency of 1.19, meaning that 1 mm s^{-1} of upward motion more than cancels the isotopic effect of 1 mm s^{-1} of entrainment. For humidity, by contrast, the counteraction efficiency is only 0.30, thereby making the isotopic imprint a far more sensitive tracer of SMOC dynamics than humidity alone.

325

Our analysis extends both ~~Our analysis extends these~~ studies by localizing the coupling mechanisms in the vertical. ~~We show that the~~ The strongest correlations between vertical velocity and both δD and humidity occur just below the subcloud layer top, ~~pinpointing—identifying~~ where mesoscale circulations ~~leave their imprint on~~ most directly influence near-surface composition. This vertical localization ~~was not resolved in either previous study and~~ sharpens the physical ~~understanding of how~~ SMOCs modulate the boundary layer. The isotopic approach also reveals that rising branches of SMOCs carry an ocean evaporation signature into the subcloud and cloud-base layers, while descending branches are associated with entrained air from the CL, yielding enhanced δD contrast between branches that far picture of SMOC-driven moisture regulation and demonstrates that ~~mesoscale ascent maintains enriched isotopic signatures characteristic of oceanic evaporation, while descent enhances the influence of entrained cloudy-layer air. The resulting isotopic contrast between ascending and descending branches~~ exceeds the corresponding ~~q -humidity~~ contrast.

~~When scaled by their observed standard deviations,~~

4.2 Why isotopes respond more strongly than humidity

~~The pronounced isotopic sensitivity arises because~~ δD responds ~~about 7.5 times more strongly to mesoscale vertical motion than does humidity, highlighting a novel asymmetry in the system's response to mesoscale variability. Small increases in entrainment lead to relatively large isotopic depletions with only modest drying. By mapping δD and q jointly onto the~~ to moisture source and processing history, whereas humidity is constrained by near-instantaneous mass balance. Mesoscale ascent modifies entrainment, cloud residence time, and interaction with condensate in ways that strongly affect isotopic composition ~~but only weakly alter total water vapor. As a result, mesoscale circulations reorganize moisture pathways and phase-change histories without producing commensurate changes in mixing ratio.~~

~~This asymmetry is evident in the joint~~ entrainment–vertical velocity ($E-W$) space, ~~we demonstrate a diagonal organization very similar where~~ δD exhibits a strong diagonal organization analogous to the SMOC moisture anomaly structure described by George et al. (2023), but with ~~stronger isotopic amplitude, confirming and quantifying the proposed moisture variance mechanism.~~

~~Our flux-form mixed-layer model provides mechanistic closure that bridges the conceptual frameworks of both studies. By parameterizing an effective entrainment frequency $\varepsilon_{\text{eff}} \propto (E - \gamma W)$, the model captures the observed asymmetry between~~ larger amplitude. While both δD and q without ad hoc tuning and reproduces the bottom-heavy variance patterns identified by George et al. (2023). This framework demonstrates that the greater sensitivity of isotopes arises naturally from the stronger ~~contrast between δ values of surface and CL sources relative to their humidity differences.~~ humidity respond to entrainment, mesoscale ascent produces large isotopic enrichment with only modest moistening. Isotopic tracers therefore expose compensation mechanisms that remain largely hidden in humidity alone.

~~Thus, while our results broadly confirm the conclusions that mixing–desiccation fails in the trade-wind regime and that SMOCs fundamentally modulate boundary layer moisture, they advance our understanding by: (1) quantifying counteraction efficiencies, (2) providing source-specific attribution of moisture variability through isotopic tracers, (3) localizing the coupling mechanisms in the vertical, and (4) offering a simple yet physically grounded model framework. Together, these findings~~

sharpen the refutation of the mixing–desiccation hypothesis, deepen our mechanistic understanding of SMOC–moisture coupling, and provide a pathway for incorporating isotope constraints into parameterizations of shallow convection and cloud feedbacks.

365 Our findings provide extensions to the theoretical frameworks for MBL water vapor isotopic composition established by Benetti et al. (2018) and more recent empirical work by Galewsky et al. (2022) and Risi et al. (2019). While Benetti et al. (2018) demonstrated that their

4.3 Relation to existing isotope frameworks

Our results extend existing theoretical and observational frameworks for marine boundary layer isotopic composition. The
370 MBL-mix model of Benetti et al. (2018) successfully reproduces isotopic observations by incorporating both evaporative flux variability variability through surface evaporation and mixing with isotopically depleted free-tropospheric air, our study air aloft. Our analysis shows that mesoscale vertical velocities motions introduce an additional layer of complexity that fundamentally modulates these mixing processes. The counteraction efficiency we observe, where 1 mm s^{-1} of upward motion counteracts the isotopic effect of 1.19 mm s^{-1} of entrainment for δD , suggests that mesoscale circulations can completely
375 overwhelm the traditional dynamical modulation of these processes, altering the effective contribution of cloudy-layer air on timescales shorter than those typically considered in two-endmember mixing framework during periods of strong vertical motion. This finding extends beyond the MBL-mix model's scope by demonstrating that the proportion of water vapor from the LFT (the r parameter in Benetti et al. (2018)) is not simply determined by entrainment rates but is dynamically modulated by mesoscale vertical velocities on timescales much shorter than typically considered frameworks.

380 The asymmetric. Similarly, the asymmetric isotopic response we document between δD and humidity to mesoscale forcing provides quantitative support for is consistent with the processes outlined in Galewsky et al. (2022), while revealing mechanisms that operate across different scales and environments. Our observations from EUREC4A show δD responding 7.5 times more strongly than humidity to mesoscale vertical motion (in σ -units), which parallels Galewsky et al. (2022)'s finding of stronger isotopic than humidity responses to decoupling in stratocumulus-topped boundary layers. However, our EUREC4A
385 results by Galewsky et al. (2022), who showed that water vapor isotopologues provide sensitivity to boundary layer mixing and decoupling processes in stratocumulus regimes that is not evident from humidity alone. Our EUREC⁴A observations demonstrate that this asymmetry sensitivity extends to the trade cumulus regime and operates on mesoscale rather than is expressed through mesoscale overturning circulations rather than solely through boundary layer decoupling timescales. The vertical localization we observe, with strongest correlations occurring just below the subcloud layer top, provides the missing
390 observed here provides a mechanistic link between the surface isotopic signatures and the shallow mesoscale overturning circulations (SMOCs) identified by George et al. (2023). This suggests that the local sources of water vapor invoked by Galewsky et al. (2022) must be understood within the context of mesoscale mesoscale circulation patterns that can transport locally evaporated, but subsequently fractionated, water vapor between different levels of but differentially processed vapor within the boundary layer.

395 Our results further advance the understanding developed by Risi et al. (2019) regarding the relative importance of surface
fluxes versus atmospheric mixing in controlling MBL isotopic composition. While Risi et al. (2019) demonstrated that boundary
layer mixing processes could explain isotopic variability without invoking large-scale horizontal transport, our study reveals
that the mixing itself is not a passive process but is actively modulated by mesoscale dynamics. The efficiency with which
vertical velocity counteracts entrainment effects (efficiency > 1.0 for δD) indicates that during periods of mesoscale ascent, the
400 traditional closure assumptions fundamentally break down. The MBL findings also complement the analysis of Risi et al. (2019)
, who emphasized the role of local mixing processes in controlling isotopic variability. We show that this mixing is dynamically
modulated rather than passive: mesoscale vertical motion alters the isotopic character of the entrained air itself by redistributing
vapor that has undergone different degrees of cloud processing. During active mesoscale periods, the boundary layer cannot
be treated as a simple two-endmember system during active mesoscale periods, as the vertical motion effectively changes
405 the isotopic composition of the entrained endmember by redistributing water vapor that has undergone different degrees of
processing within the boundary layer.

This finding reconciles the apparent contradiction between Risi et al. (2019)'s emphasis on local processes and the need to
explain isotopic depletions that exceed what simple surface-atmosphere exchange can produce

4.4 Broader implications and limitations

410 The strong isotopic sensitivity to mesoscale vertical motion provides an observational constraint on boundary layer coupling
that is not available from humidity alone. Large-eddy simulations of shallow convection often exhibit weak mesoscale signals in
subcloud-layer humidity due to efficient turbulent mixing (Bretherton and Blossey, 2017; Janssens et al., 2023). Our isotopic
observations demonstrate that mesoscale dynamics nevertheless leave a clear imprint on near-surface composition, indicating
that δD is a sensitive tracer of mesoscale-surface coupling even when humidity anomalies are muted.

415 While our analysis focuses on mesoscale circulations, cold pools and precipitation also influence boundary layer structure
during EUREC⁴A (Touzé-Peiffer et al., 2022; Radtke et al., 2022). The strongest isotopic-vertical velocity correlations occur
near 500–600 m, generally above the shallowest layers most strongly affected by cold-pool outflows. This suggests that the
isotopic signal primarily reflects deeper mesoscale overturning rather than near-surface cold-pool dynamics, though future
work explicitly incorporating cold-pool diagnostics would help further separate these influences.

420 The integration of our results with these previous studies reveals Overall, our results show that the marine boundary layer iso-
topic composition emerges from a balance between surface evaporation (Craig-Gordon effects) the combined effects of surface
evaporation, entrainment mixing (Benetti et al. (2018) framework), boundary layer decoupling processes (Galewsky et al. (2022)
mechanisms), cloud processing, and mesoscale circulation modulation (our new contribution). Rather than invalidating previous
work, our study demonstrates that these assumptions hold only during quiescent periods and must be replaced by a more
425 dynamic framework during periods of significant mesoscale activity. That mesoscale processes dominate over entrainment
in determining surface isotopic signatures while showing weaker control over humidity suggests that isotopic measurements
provide a uniquely sensitive probe. These processes are not independent: mesoscale vertical motion dynamically reshapes
mixing pathways without producing proportional changes in humidity. This asymmetric response highlights the value of

isotopic measurements as probes of mesoscale dynamics ~~that cannot be detected through humidity observations alone~~ and provides a framework for incorporating isotope constraints into representations of shallow convection and cloud feedbacks.

5 Conclusions

The goal of this study was to quantify how mesoscale vertical motions modulate marine boundary layer moisture and isotopic composition in the ~~trade-wind-trade-wind~~ regime, and to test ~~the mixing-desiccation~~ interpretations of the mixing-desiccation hypothesis using water vapor isotopologue observations from EUREC⁴A.

435 ~~We found~~ Our main findings are as follows:

1. Water vapor ~~δD responds approximately 7.5 times more strongly to~~ δD and mixing ratio exhibit distinct sensitivities to mesoscale circulation. While humidity variability is primarily controlled by entrainment, δD is more strongly modulated by mesoscale vertical velocity variations than humidity itself (when normalized by observed standard deviations), with δD showing a linear sensitivity of $3.72 \sigma_{\delta D}$ per cm s^{-1} compared to $0.49 \sigma_q$ per cm s^{-1} for specific humidity, demonstrating that isotopic composition encodes mesoscale dynamics more clearly than humidity alone.
2. ~~Mesoscale upward motion counteracts entrainment-driven isotopic depletion with an efficiency of 1.19, meaning 1 mm s^{-1} of vertical velocity more than cancels the isotopic effect of 1 mm s^{-1} of entrainment, while the counteraction efficiency~~ Using standardized regression coefficients, we find that mesoscale vertical velocity exerts a stronger relative influence on δD than entrainment does, with a counteraction efficiency of $\eta_{\delta D} \approx 1.5$. In contrast, the corresponding efficiency for humidity is ~~only 0.30~~ much smaller ($\eta_q \approx 0.25$), highlighting a pronounced asymmetry in the response of isotopic composition and total moisture to mesoscale forcing.
3. The strongest correlations between vertical velocity and both ~~δD~~ δD ($r \approx 0.52$) and mixing ratio ($r \approx 0.39$) occur within approximately ± 200 m of the subcloud layer top, ~~pinpointing~~ identifying the vertical region where mesoscale circulations exert their primary influence on surface ~~most directly influence near-surface~~ composition.
4. Periods of enhanced entrainment ~~consistently coincide~~ are consistently associated with more negative ~~δD~~ δD values and lower mixing ratios, ~~while~~ whereas periods of mesoscale ascent correspond to less negative ~~δD and higher humidity,~~ demonstrating δD and modest moistening. Together, these relationships reveal a systematic organization of boundary layer states across ~~the entrainment-vertical velocity parameter space~~ entrainment-vertical velocity space, consistent with shallow mesoscale overturning circulations.
- 455 5. A steady-state, flux-form mixed-layer model reproduces the observed asymmetric responses, ~~confirming~~ of δD and humidity without ad hoc tuning. The model shows that isotopic composition is ~~more sensitive~~ intrinsically more sensitive than humidity to changes in ~~source mixing ratios than bulk humidity,~~ thereby the relative contributions of surface and cloudy-layer sources, providing mechanistic closure for the ~~counteraction effects observed in the trade-wind regime~~ observed counteraction between entrainment and mesoscale ascent.

460 While the relatively small natural variability in δD Although the natural variability of δD during the campaign means that the
 precise is modest and quantitative sensitivities should be interpreted with caution therefore be interpreted cautiously, the conver-
 465 gence of multiple diagnostics and agreement with the mechanistic model give confidence in the observational diagnostics and
 model behavior supports a robust qualitative conclusion: isotopic composition provides a far more water vapor isotopologues
 provide a sensitive tracer of mesoscale circulations than humidity alone in the trade-wind boundary layer that is not accessible
 from humidity measurements alone. These results refine interpretations of the mixing-desiccation hypothesis by showing
 that mesoscale vertical motions reorganize moisture pathways and source contributions without producing commensurate
 changes in total water vapor, underscoring the value of isotopic constraints for understanding boundary layer dynamics and
 cloud-circulation coupling.

470 Data availability. EUREC⁴A water vapor isotope data from R/V Meteor and HALO/P3 dropsonde data from the JOANNE dataset are
 publicly available through the EUREC⁴A data portal at <https://eurec4a.eu/data>.

Appendix A: Flux-Form Mixed-Layer Model Formulation

A1 Model Overview Framework

We use employ a steady-state, flux-form mixed-layer model to represent the moisture and isotopic budgets of resolve the budget
 of specific humidity (q_{BL}) and isotopic ratio (R_{BL}) within the subcloud layer (SCL) in the tropical marine boundary layer. The
 475 model is spatially homogeneous in the horizontal, has a fixed SCL height treats the SCL as a well-mixed slab of depth h , and
 resolves only bulk mean quantities: the specific humidity q_{BL} and the isotopic composition δ_{BL} of boundary-layer water vapor.
 The SCL exchanges water and isotopes that interacts with three reservoirs: the ocean surface, the free troposphere/cloud layer
 above, and a hydrometeor reservoir (rain/cloud droplets) driven by mesoscale ascent. Note that we use the subscript 'BL' to
 denote bulk properties of the well-mixed SCL.

480 **Surface source:** evaporation from the ocean, with specific humidity q_{flux} and isotopic composition δ_{flux} . **Cloudy-Layer
 (CL) source:** entrainment of air from above the top of the SCL, with q_{FT} and δ_{FT} . **Ventilation sink:** large-scale advection or
 lateral mixing at rate

A2 Moisture Budget

485 The steady-state mass budget for specific humidity q_{BL} is defined by the balance between surface evaporation and entrainment
 drying:

$$0 = F_E + F_{ent}, \tag{A1}$$

where F_E is the surface evaporative mass flux and F_{ent} is the net entrainment flux. We parameterize the surface flux as a relaxation toward saturation:

$$F_E = \lambda(q_s - q_{\text{BL}}), \quad (\text{A2})$$

490 where λ (s^{-1}),

The model tracks the competition between these fluxes as modulated by the entrainment rate E and the mesoscale vertical velocity W . We introduce an “effective” entrainment frequency ε_{eff} to capture the modulation of entrainment by mesoscale motions.

A3 Governing Equations

495 Let q_{BL} be the boundary-layer specific humidity in g kg^{-1} , and R_{BL} the isotopic ratio (D/H) in absolute units. The steady-state moisture budget is a surface coupling timescale and q_s is the saturation specific humidity at sea surface temperature (SST) and pressure. Note that by definition $q_{\text{BL}} = \mathcal{H}q_s$, where \mathcal{H} is the relative humidity (normalized to 1). Therefore, Eq. (A2) can be written as $F_E = \lambda q_s(1 - \mathcal{H})$.

The entrainment flux is parameterized as:

$$500 \quad 0F_{\text{ent}} = \lambda q_{\text{flux}} - q_{\text{BL}} + \varepsilon_{\text{eff}}(q_{\text{FT}} - q_{\text{BL}}), \quad (\text{A3})$$

where q_{FT} is the humidity of the overlying cloudy layer. To represent the modulation of boundary layer ventilation by mesoscale circulations, we define an effective entrainment rate ε_{eff} :

$$\varepsilon_{\text{eff}} = \max\left(\frac{E - \gamma W}{h}, 0\right). \quad (\text{A4})$$

505 Here, E and W are the mean entrainment velocity and the mesoscale vertical velocity (both in m s^{-1} , h in m), and γ is a dimensionless “counteraction efficiency” relating vertical velocity to effective entrainment reduction. In the calculations presented here, $\gamma = 1.0$. Negative values of ε_{eff} are clipped to zero.

Solving (??) for q_{BL} an empirical counteraction efficiency which controls the degree to which ascent offsets entrainment-driven ventilation. Combining these terms, we solve for the steady-state humidity:

$$q_{\text{BL}} = \frac{q_{\text{flux}} \lambda + q_{\text{FT}} \varepsilon_{\text{eff}}}{\lambda + \varepsilon_{\text{eff}}} \frac{\lambda q_s + \varepsilon_{\text{eff}} q_{\text{FT}}}{\lambda + \varepsilon_{\text{eff}}}. \quad (\text{A5})$$

510 For the runs shown, q_{flux} is approximated by the saturation mixing ratio at the sea-surface temperature and pressure, $q_s(\text{SST}, p)$, computed with the Tetens formula for $e_s(T)$ and

A3 Isotopic Budget

The isotopic budget is solved for the isotopic ratio $R = D/H$. We enforce strict consistency between the mass fluxes defined above and the corresponding isotopic fluxes. Under steady-state conditions, the isotopic budget is written as

$$515 \quad \underline{q_s} \cdot 0 = \frac{\varepsilon e_s}{p - e_s} F_{\text{iso,E}} + F_{\text{iso,ent}} + F_{\text{iso,ex}}, \quad \varepsilon = 0.622. \quad (\text{A6})$$

where the terms represent surface evaporation, entrainment from the cloudy layer into the subcloud layer, and an effective cloud-rain isotopic exchange process, respectively. No additional export, dilution, or storage terms are included.

A4 Isotopic Balance

Let $R = 1 + \delta/1000$ be the conversion from δ notation (in ‰) to absolute isotopic ratio normalized to VSMOW. Denote R_{flux} and R_{FT} as the source isotopic ratios corresponding to δ_{flux} and δ_{FT} . Isotopic ratios are converted to delta notation relative to VSMOW via

$$520 \quad \delta = 1000 \left(\frac{R}{R_{\text{VSMOW}}} - 1 \right), \quad (\text{A7})$$

where R_{VSMOW} is the standard isotopic ratio.

The steady-state isotopic mass balance is

$$525 \quad 0 = \lambda (q_{\text{flux}} R_{\text{flux}} - q_{\text{BL}} R_{\text{BL}}) + \varepsilon_{\text{eff}} (q_{\text{FT}} R_{\text{FT}} - q_{\text{BL}} R_{\text{BL}}).$$

Solving for R_{BL}

A3.1 Consistent Craig-Gordon Evaporation

The isotopic evaporative flux is expressed as the product of the bulk mass flux and the isotopic ratio of the evaporating vapor, R_E :

$$530 \quad \underline{R_{\text{BL}}} F_{\text{iso,E}} = \frac{\lambda q_{\text{flux}} R_{\text{flux}} + \varepsilon_{\text{eff}} q_{\text{FT}} R_{\text{FT}}}{(\lambda + \varepsilon_{\text{eff}}) q_{\text{BL}}} F_E \cdot R_E. \quad (\text{A8})$$

The model output δ_{BL} is then We adopt the linear-resistance form of the Craig-Gordon model (Craig and Gordon, 1965),

$$\delta_{\text{BL}} = 1000 (R_{\text{BL}} - 1) = \frac{R_{\text{oc}}/\alpha_{\text{eq}} - \mathcal{H} R_{\text{BL}}}{\alpha_k (1 - \mathcal{H})}, \quad (\text{A9})$$

where R_{oc} is the ocean surface isotopic ratio, α_{eq} is the equilibrium fractionation factor at the sea surface temperature, α_k is the kinetic fractionation factor, and \mathcal{H} is the near-surface relative humidity defined at the sea surface temperature.

535 For the surface source isotopic composition δ_{flux} , the model by default uses the Substituting the bulk flux expression $F_E = \lambda q_s (1 - \mathcal{H})$ into the isotopic flux formulation yields

$$F_{\text{iso,E}} = [\lambda q_s (1 - \mathcal{H})] \cdot \left[\frac{R_{\text{oc}}/\alpha_{\text{eq}} - \mathcal{H} R_{\text{BL}}}{\alpha_k (1 - \mathcal{H})} \right] = \frac{\lambda q_s}{\alpha_k} \left(\frac{R_{\text{oc}}}{\alpha_{\text{eq}}} - \mathcal{H} R_{\text{BL}} \right), \quad (\text{A10})$$

demonstrating explicit cancellation of the $(1 - \mathcal{H})$ dependence.

540 This formulation ensures that the isotopic flux is fully consistent with the mass budget and avoids artificial singular behavior as $\mathcal{H} \rightarrow 1$.

The evaporative isotopic flux is parameterized using a simplified Craig–Gordon formulation, which depends on SST, relative humidity, and pressure. With the campaign-state values (SST = 27.3°C, RH = 0.716, $p = 101325$ Pa), this yields $\delta_{\text{flux}} \approx -74.7\%$ framework that assumes a single effective kinetic fractionation factor and neglects explicit aerodynamic resistance terms. This formulation is intended to capture first-order isotopic effects under near-surface marine boundary layer conditions rather than to represent a complete microphysical description of evaporation.

A3.2 Entrainment and Exchange

The entrainment isotopic flux follows directly from the mass flux formulation,

$$F_{\text{iso,ent}} = \varepsilon_{\text{eff}} (q_{\text{FT}} R_{\text{FT}} - q_{\text{BL}} R_{\text{BL}}), \quad (\text{A11})$$

550 where ε_{eff} is the effective entrainment velocity and subscripts FT and BL denote free-tropospheric and boundary-layer air, respectively.

We introduce an additional exchange term, $F_{\text{iso,ex}}$, to parameterize isotopic equilibration between boundary-layer vapor and hydrometeors (cloud droplets or rain) during mesoscale ascent. This process is represented as a relaxation of boundary-layer vapor toward a target isotopic ratio R_{rain} ,

$$F_{\text{iso,ex}} = k_{\text{ex}} q_{\text{BL}} (R_{\text{rain}} - R_{\text{BL}}). \quad (\text{A12})$$

555 The exchange term $F_{\text{iso,ex}}$ represents an effective parameterization of isotopic re-equilibration associated with precipitation and cloud processing, in which net vapor mass changes may be small even though isotopic exchange occurs through repeated phase changes. As such, this term modifies the isotopic composition of boundary-layer vapor without introducing an explicit moisture source or sink.

A4 Parameter Values Used

560 The exchange rate k_{ex} (s^{-1}) is parameterized as a bounded logistic function of mesoscale vertical velocity,

$$k_{\text{ex}}(W) = \frac{k_{\text{max}}}{1 + \exp(-W/w_{\text{width}})}, \quad (\text{A13})$$

reflecting the onset and intensification of cloud and precipitation processing during upward motion. The dependence of k_{ex} on W should therefore be interpreted as a proxy for cloud fraction and precipitation activity, rather than as a direct representation of a specific microphysical mechanism.

565 For the runs shown in the main-text figures:-

A4 Solution

Equation (A6) is linear in R_{BL} . Separating terms into sources (independent of R_{BL}) and sinks (proportional to R_{BL}):

$$\text{Source} = \frac{\lambda q_s}{\alpha_k \alpha_{\text{eq}}} R_{\text{oc}} + \varepsilon_{\text{eff}} q_{\text{FT}} R_{\text{FT}} + k_{\text{ex}} q_{\text{BL}} R_{\text{rain}}, \quad (\text{A14})$$

$$\text{Sink Coeff.} = \frac{\lambda q_s \mathcal{H}}{\alpha_k} + \varepsilon_{\text{eff}} q_{\text{BL}} + k_{\text{ex}} q_{\text{BL}}. \quad (\text{A15})$$

570 The steady-state ratio is $R_{\text{BL}} = \text{Source}/\text{Sink Coeff.}$, which is converted to δ notation via $\delta_{\text{BL}} = 1000(R_{\text{BL}} - 1)$.

A5 Parameter Values

Parameters used in the standard run are listed below. Equilibrium fractionation α_{eq} is calculated following Majoube (1971), and the kinetic fractionation factor α_k is set to 1.0126 following Merlivat and Jouzel (1979) for the rough surface regime.

- ~~$h = 650 \text{ m}$~~
- 575 ~~$\gamma = 1.0$~~
- ~~$q_{\text{FT}} = 3 \text{ g kg}^{-1}$~~
- ~~$\delta_{\text{FT}} = -150 \text{ ‰}$~~
- ~~δ_{flux} from Craig–Gordon with **Environmental**: SST = 27.3°C, RH = 0.716, $p = 101325 \text{ Pa}$, giving $\approx -74.7 \text{ ‰}$ $p = 1013.25 \text{ hPa}$, $h = 700 \text{ m}$.~~
- 580 ~~$\lambda = 0.10 \text{ day}$ **Coupling Timescale**: $\lambda = 1.16 \times 10^{-6} \text{ s}^{-1}$ (converted to ≈ 10 days) corresponding to a surface moistening timescale of ≈ 10 days).~~
- ~~**End Members**: $q_{\text{FT}} = 13.0 \text{ g kg}^{-1}$ (in computations), $\delta_{\text{FT}} = -90 \text{ ‰}$, $\delta_{\text{rain}} = -70 \text{ ‰}$.~~
- ~~E and W explored in ranges: $E \in [10, 35] \text{ mm}$ **Entrainment Closure**: $\gamma = 0.30$.~~
- 585 ~~**Optimized Exchange**: $k_{\text{max}} \approx 10^{-4} \text{ s}^{-1}$, $W \in [-10, 10] \text{ m s}^{-1}$, $w_{\text{width}} \approx 5.0 \text{ mm s}^{-1}$ (optimized within physically reasonable bounds).~~

We emphasize that this formulation is intended to demonstrate the existence of a physically plausible parameter regime capable of reproducing the observed contrast between humidity and isotopic gradients, rather than to identify a unique or optimal representation of boundary layer processes.

Author contributions. JG conceived the study, analyzed the data, developed the mixed-layer model, and wrote the manuscript. SL processed the isotopic data and contributed to the analysis. Both authors contributed to the interpretation and editing of the manuscript.

Competing interests. The authors declare no competing interests.

Acknowledgements. The authors used artificial intelligence (ChatGPT, OpenAI, 2025) to assist with coding the mixed-layer model and with drafting some initial text. All code, results, and manuscript content were thoroughly checked, validated, and revised by the authors, who take full responsibility for the accuracy and interpretation of the work. We acknowledge the EUREC4A campaign organizers and participants, particularly the crew of R/V Meteor and the HALO [and P3](#) aircraft operations team. This work was supported by the U.S. National Science Foundation under grant AGS-1853353. We thank the German Research Foundation (DFG) for support of the [EUREC4A](#) [EUREC⁴A](#) campaign under grant 264907654.

References

- Albright, A. L., Bony, S., Stevens, B., and Vogel, R.: Observed subcloud-layer moisture and heat budgets in the trades, *Journal of the Atmospheric Sciences*, 79, 2363–2385, <https://doi.org/10.1175/JAS-D-21-0337.1>, 2022.
- Bailey, A., Aemisegger, F., Villiger, L., Los, S. A., Reverdin, G., Galewsky, J., Noone, D., and Steen-Larsen, H. C.: Isotopic measurements in water vapor, precipitation, and seawater during EUREC⁴A, *Earth System Science Data*, 15, 465–495, <https://doi.org/10.5194/essd-15-465-2023>, 2023.
- Benetti, M., Aloisi, G., Reverdin, G., Risi, C., and Sèze, G.: Importance of boundary layer mixing for the isotopic composition of surface vapor over the subtropical North Atlantic Ocean, *Journal of Geophysical Research: Atmospheres*, 123, 2442–2461, <https://doi.org/10.1002/2017JD027593>, 2018.
- Bony, S. and Dufresne, J.-L.: Marine boundary layer clouds at the heart of tropical cloud feedback uncertainties in climate models, *Geophysical Research Letters*, 32, L20 806, <https://doi.org/10.1029/2005GL023851>, 2005.
- Bony, S. and Stevens, B.: Measuring area-averaged vertical motions with dropsondes, *Journal of the Atmospheric Sciences*, 76, 767–783, <https://doi.org/10.1175/JAS-D-18-0141.1>, 2019.
- Bony, S., Stevens, B., Ament, F., Albright, A., Acquistapace, C., Aemisegger, F., Farrell, D., Galewsky, J., Giez, A., Lenschow, D., Nuijens, L., Rauber, R., Röttenbacher, J., Schnitt, S., Schulz, H., Vial, J., Winker, D., and Zhang, L.: EUREC⁴A: A field campaign to elucidate the couplings between clouds, convection and circulation, *Surveys in Geophysics*, 38, 1529–1568, <https://doi.org/10.1007/s10712-017-9428-0>, 2017.
- Bretherton, C. S. and Blossey, P. N.: Understanding Mesoscale Aggregation of Shallow Cumulus Convection Using Large-Eddy Simulation, *Journal of Advances in Modeling Earth Systems*, 9, 2798–2821, <https://doi.org/10.1002/2017MS000981>, 2017.
- Craig, H. and Gordon, L. I.: Deuterium and oxygen-18 variations in the ocean and the marine atmosphere, in: *Stable Isotopes in Oceanographic Studies and Paleotemperatures*, edited by Tongiorgi, E., pp. 9–130, Consiglio Nazionale delle Ricerche, Laboratorio di Geologia Nucleare, Pisa, Italy, 1965.
- Galewsky, J., Steen-Larsen, H. C., Field, R. D., Worden, J., Risi, C., and Schneider, M.: Stable isotopes in atmospheric water vapor and applications to the hydrologic cycle, *Reviews of Geophysics*, 54, 809–865, <https://doi.org/10.1002/2015RG000512>, 2016.
- Galewsky, J., Jensen, M. P., and Delp, J.: Marine Boundary Layer Decoupling and the Stable Isotopic Composition of Water Vapor, *Journal of Geophysical Research: Atmospheres*, 127, e2021JD035 470, <https://doi.org/10.1029/2021JD035470>, 2022.
- George, G., Stevens, B., Bony, S., Pincus, R., Fairall, C., Schulz, H., Kölling, T., Kalen, Q. T., Klingebiel, M., Konow, H., Lundry, A., Prange, M., and Radtke, J.: JOANNE: Joint dropsonde observations of the atmosphere in tropical North Atlantic meso-scale environments, *Earth System Science Data*, 13, 5253–5272, <https://doi.org/10.5194/essd-13-5253-2021>, 2021.
- George, G., Stevens, B., Bony, S., Vogel, R., and Naumann, A. K.: Widespread shallow mesoscale circulations observed in the trades, *Nature Geoscience*, 16, 584–589, <https://doi.org/10.1038/s41561-023-01215-1>, 2023.
- Janssens, M., Vilà-Guerau de Arellano, J., van Heerwaarden, C. C., de Roode, S. R., Siebesma, A. P., and Glassmeier, F.: Nonprecipitating Shallow Cumulus Convection Is Intrinsically Unstable to Length Scale Growth, *Journal of the Atmospheric Sciences*, 80, 849–870, <https://doi.org/10.1175/JAS-D-22-0111.1>, 2023.
- Konow, H., Ewald, F., George, G., Jacob, M., Klingebiel, M., Kölling, T., Luebke, A. E., Mieslinger, T., Pörtge, V., Radtke, J., Schäfer, M., Schulz, H., Vogel, R., Wirth, M., Bony, S., Crewell, S., Ehrlich, A., Forster, L., Giez, A., Göttsche, F., Groß, S., Gutleben, M., Hagen, M., Hirsch, L., Jansen, F., Lang, T., Mayer, B., Mech, M., Prange, M., Schnitt, S., Vial, J., Walbröl, A., Wendisch, M., Wolf, K., Zinner, T.,

- 635 Zöger, M., Ament, F., and Stevens, B.: EUREC⁴A's HALO, *Earth System Science Data*, 13, 5545–5563, <https://doi.org/10.5194/essd-13-5545-2021>, 2021.
- Lenschow, D. H., Krummel, P. B., and Siems, S. T.: Measuring Entrainment, Divergence, and Vorticity on the Mesoscale from Aircraft, *Journal of Atmospheric and Oceanic Technology*, 16, 1384–1400, [https://doi.org/10.1175/1520-0426\(1999\)016<1384:MEDAVO>2.0.CO;2](https://doi.org/10.1175/1520-0426(1999)016<1384:MEDAVO>2.0.CO;2), 1999.
- 640 Lenschow, D. H., Savic-Jovicic, V., and Stevens, B.: Divergence and vorticity from aircraft air motion measurements, *Journal of Atmospheric and Oceanic Technology*, 24, 2062–2072, <https://doi.org/10.1175/2007JTECHA940.1>, 2007.
- Lilly, D. K.: Models of cloud-topped mixed layers under a strong inversion, *Quarterly Journal of the Royal Meteorological Society*, 94, 292–309, <https://doi.org/10.1002/qj.49709440106>, 1968.
- Majoube, M.: Fractionnement en oxygène 18 et en deutérium entre l'eau et sa vapeur, *Journal de Chimie Physique*, 68, 1423–1436, <https://doi.org/10.1051/jcp/1971681423>, 1971.
- 645 Merlivat, L. and Jouzel, J.: Global climatic interpretation of the deuterium-oxygen 18 relationship for precipitation, *Journal of Geophysical Research: Oceans*, 84, 5029–5033, <https://doi.org/10.1029/JC084iC08p05029>, 1979.
- Pincus, R., Fairall, C. W., Bailey, A., Chuang, P., de Boer, G., Doyle, J., Fuchs, D., Galewsky, J., Ghate, V., Greatbatch, R., Greenslade, C., Grise, K., Haines, S., Haynes, J. M., Heffernan, J., Isarra, A., Knuth, F., Lundry, A., Nester, A., Noone, D., Pfister, L., Quinn, P. K., Rajib, Z., Richard, E., Royer, H., Schulz, H., Sorooshian, A., Speingys, N., Spangler, C., Sullivan, S., Tjernström, M., Turnbull, J., Wang, H., Witte, M. K., and Zuidema, P.: Observations from the NOAA P-3 aircraft during ATOMIC, *Earth System Science Data*, 13, 3281–3296, <https://doi.org/10.5194/essd-13-3281-2021>, 2021.
- 650 Radtke, J., Naumann, A. K., Hagen, M., and Ament, F.: The relationship between precipitation and its spatial pattern in the trades observed during EUREC⁴A, *Quarterly Journal of the Royal Meteorological Society*, 148, 1913–1928, <https://doi.org/10.1002/qj.4284>, 2022.
- 655 Risi, C., Hourdin, F., Cattiaux, J., Steen-Larsen, H. C., Wong, C. S., Galewsky, J., Lacour, J.-L., Bonne, J.-L., Clerbaux, C., Coheur, P.-F., Hurtmans, D., and Worden, J.: The water isotopic version of the LMDZ general circulation model, *Atmospheric Chemistry and Physics*, 19, 12 235–12 263, <https://doi.org/10.5194/acp-19-12235-2019>, 2019.
- Risi, C., Muller, C., and Blossey, P. N.: What Controls the Water Vapor Isotopic Composition Near the Surface of Tropical Oceans? Results from an Analytical Model Constrained by Large-Eddy Simulations, *Journal of Advances in Modeling Earth Systems*, 12, e2020MS002 106, <https://doi.org/10.1029/2020MS002106>, 2020.
- 660 Sherwood, S. C., Bony, S., and Dufresne, J.-L.: Spread in model climate sensitivity traced to atmospheric convective mixing, *Nature*, 505, 37–42, <https://doi.org/10.1038/nature12829>, 2014.
- Stevens, B., Bony, S., Farrell, D., Ament, F., Blyth, A., Fairall, C., Karstensen, J., Quinn, P. K., Speich, S., Acquistapace, C., Aemisegger, F., Albright, A. L., Bellenger, H., Bodenschatz, E., Caesar, K.-A., Chewitt-Lucas, R., de Boer, G., Delanoë, J., Denby, L., Ewald, F., Fildier, B., Forde, M., George, G., Gross, S., Hagen, M., Hausold, A., Heywood, K. J., Hirsch, L., Jacob, M., Jansen, F., Kinne, S., Klocke, D., Kölling, T., Konow, H., Lathon, M., Mohr, W., Naumann, A. K., Nuijens, L., Olivier, L., Pincus, R., Pöhlker, M., Reverdin, G., Roberts, G., Schnitt, S., Schulz, H., Siebesma, A. P., Stephan, C. C., Sullivan, P., Touzé-Peiffer, L., Vial, J., Vogel, R., Zuidema, P., Alexander, N., Alves, L., Arixi, S., Asmath, H., Bagheri, G., Baier, K., Bailey, A., Baranowski, D., Baron, A., Barrau, S., Barrett, P. A., Batier, F., Behrendt, A., Bendinger, A., Beucher, F., Bigorre, S., Blades, E., Blossey, P., Bock, O., Böing, S., Bossler, P., Bourras, D., Bouruet-Aubertot, P., Bower, K., Branellec, P., Branger, H., Brennan, M., Brewer, A., Brilouet, P.-E., Brüggemann, B., Buehler, S. A., Burke, E., Burton, R., Calmer, R., Canonici, J.-C., Carton, X., Cato Jr., G., Charles, J. A., Chazette, P., Chen, Y., Chilinski, M. T., Choulaton, T., Chuang, P., Clarke, S., Coe, H., Cornet, C., Coutris, P., Couvreux, F., Crewell, S., Cronin, T., Cui, Z., Cuypers, Y., Daley, A., Damerell,

G. M., Dauhut, T., Deneke, H., Desbios, J.-P., Dörner, S., Donner, S., Douet, V., Drushka, K., Dütsch, M., Ehrlich, A., Emanuel, K., Emmanouilidis, A., Etienne, J.-C., Etienne-Leblanc, S., Faure, G., Feingold, G., Ferrero, L., Fix, A., Flamant, C., Flatau, P. J., Foltz, 675 G. R., Forster, L., Furtuna, I., Gadian, A., Galewsky, J., Gallagher, M., Gallimore, P., Gaston, C., Gentemann, C., Geyskens, N., Giez, A., Gollop, J., Gourirand, I., Gourbeyre, C., de Graaf, D., de Groot, G. E., Grosz, R., Güttler, J., Gutleben, M., Hall, K., Harris, G., Helfer, K. C., Henze, D., Herbert, C., Holanda, B., Ibanez-Landeta, A., Intrieri, J., Iyer, S., Julien, F., Kalesse, H., Kazil, J., Kellman, A., Kidane, A. T., Kirchner, U., Klingebiel, M., Körner, M., Kremper, L. A., Kretzschmar, J., Krüger, O., Kumala, W., Kurz, A., L'Hégaret, P., Labaste, M., Lachlan-Cope, T., Laing, A., Landschützer, P., Lang, T., Lange, D., Lange, I., Laplacette, C., Lavik, G., Laxenaire, R., Le Bihan, C., 680 Leandro, M., Lefevre, N., Lena, M., Lenschow, D., Li, Q., Lloyd, G., Los, S., Losi, N., Lovell, O., Luneau, C., Makuch, P., Malinowski, S., Manta, G., Marinou, E., Marsden, N., Masson, S., Maury, N., Mayer, B., Mayers-Als, M., Mazel, C., McGeary, W., McWilliams, J. C., Mech, M., Mehlmann, M., Meroni, A. N., Mieslinger, T., Minikin, A., Minnett, P., Möller, G., Morfa Avalos, Y., Muller, C., Musat, I., Napoli, A., Neuberger, A., Noisel, C., Noone, D., Nordsiek, F., Nowak, J. L., Oswald, L., Parker, D. J., Peck, C., Person, R., Philippi, M., Plueddemann, A., Pöhlker, C., Pörtge, V., Pöschl, U., Pologne, L., Posyniak, M., Prange, M., Quiñones Meléndez, E., Radtke, J., Ramage, 685 K., Reimann, J., Renault, L., Reus, K., Reyes, A., Ribbe, J., Ringel, M., Ritschel, M., Rocha, C. B., Rochetin, N., Röttenbacher, J., Rollo, C., Royer, H., Sadoulet, P., Saffin, L., Sandiford, S., Sandu, I., Schäfer, M., Schemann, V., Schirmacher, I., Schlenczek, O., Schmidt, J., Schröder, M., Schwarzenboeck, A., Sealy, A., Senff, C. J., Serikov, I., Shohan, S., Siddle, E., Smirnov, A., Späth, F., Spooner, B., Stolla, M. K., Szkółka, W., de Szoeko, S. P., Tarot, S., Tetoni, E., Thompson, E., Thomson, J., Tomassini, L., Totems, J., Ubele, A. A., Villiger, L., von Arx, J., Wagner, T., Walther, A., Webber, B., Wendisch, M., Whitehall, S., Wiltshire, A., Wing, A. A., Wirth, M., Wiskandt, J., 690 Wolf, K., Worbes, L., Wright, E., Wulfmeyer, V., Young, S., Zhang, C., Zhang, D., Ziemann, F., Zinner, T., and Zöger, M.: EUREC⁴A: An Atlantic trade-wind cloud experiment, *Earth System Science Data*, 13, 4067–4119, <https://doi.org/10.5194/essd-13-4067-2021>, 2021.

Stull, R. B.: The energetics of entrainment across a density interface, *Journal of the Atmospheric Sciences*, 33, 1260–1267, [https://doi.org/10.1175/1520-0469\(1976\)033<1260:TEOEAD>2.0.CO;2](https://doi.org/10.1175/1520-0469(1976)033<1260:TEOEAD>2.0.CO;2), 1976.

Touzé-Peiffer, L., Vogel, R., and Rochetin, N.: Cold pools observed during EUREC⁴A: detection and characterization from atmospheric 695 soundings, *Journal of Applied Meteorology and Climatology*, 61, 593–610, <https://doi.org/10.1175/JAMC-D-21-0048.1>, 2022.

Vogel, R., Albright, A. L., Vial, J., George, G., Stevens, B., and Bony, S.: Strong cloud–circulation coupling explains weak trade cumulus feedback, *Nature*, 612, 696–700, <https://doi.org/10.1038/s41586-022-05364-y>, 2022.